Janus-like Fe_3O_4/PDA-vesicles with Broadening Microwave Absorption Bandwidth†

Xiaofeng Shi, Zhengwang Liu, Wenbin You, Xuebing Zhao and Renchao Che*

Laboratory of Advanced Materials, Department of Materials Science, Collaborative Innovation Center of Chemistry for Energy Materials, Department of Chemistry, Fudan University, 220 Handan Road, Shanghai 200438, China
** E-mail: rcche@fudan.edu.cn*

S1: The details of conventional electromagnetic measurements

Microwave absorption properties were studied by mixing homogeneously the epoxy resin (EP) with as-prepared samples in a weight ratio of 5:1, the reflection loss of samples was measured through a portion of the composites coating an aluminum substrate (180mm x 180mm) with a thickness of 2 mm, the remaining portion was molded into the hollow pipe with dimensions of 3 mm x 7 mm x 2 mm to test complex permeability and permittivity, the complex relative permittivity and permeability were measured with an HP8510C vector network analyzer in the 2-18 GHz range. Derived from transmission line theory, the reflection loss (RL) values were determined with the following equations:

$$Z_{\text{in}} = \sqrt{\frac{\mu_r}{\varepsilon_r}} \tanh[-j(\frac{2\pi f d}{c})\sqrt{\mu_r \cdot \varepsilon_r}]$$

$$RL(dB) = -20 \log_{10}\left|(Z_{in} - 1) / (Z_{in} + 1)\right|$$

Where Z_{in} is the input impedance of the absorber, μ_r and ε_r are the relative permeability and permittivity, respectively. f is the frequency of microwave, c is the velocity of light, d is the coating thickness of the absorber.

S2: More discussion about Electron holography

The quantitative information on the electrostatic and magnetic field for the material could be obtained by off-axis electron holography with nanoscale resolution. The phase shift of the electron wave through the material is sensitive to the mean internal potential and in-plane magnetic induction. The accurate sideband position are obtained by the Fourier transform. Based on the sideband, the hologram is inverse-Fourier-transformed to get the phase change of the electron wave through the sample. The phase change of the electron wave in the vacuum area outside the sample is caused by the magnetic field on sample surface. During the course of the experiment, the information of the sample thickness isn't considered. Electron holographic reconstruction map shows the stray magnetic field outer of the nanospheres. The phase is described in one dimension ignoring dynamical diffraction effects by

$$\phi(x) = \left(\frac{2\pi}{\lambda}\right)\left(\frac{E + E_0}{E(E + 2E_0)}\right)\int V(x, z)\mathrm{d}z - \left(\frac{e}{\hbar}\right) \times \iint B_{\perp}(x, z)\mathrm{d}x\mathrm{d}z$$

Where *z* is the incident beam direction, *x* is a direction in the plane of the sample, $B_{\perp}$ is the magnetic induction perpendicular to both *x* and *z*, *V* is the mean inner potential, λ is the wavelength and E and E_0 are the kinetic and rest mass energies of the incident electron, respectively.

S3. The analysis of XPS and FTIR spectrum

The PDA vesicle and Fe_3O_4 core were verified by Fourier transform infrared (FT-IR). As shown in Fig S, the strong peak at 576.7 cm^{-1} corresponds to the Fe-O band. The absorption peak at 1234.4 cm^{-1} is the C-O stretching vibration and the band appearing at 1504.4 cm-1 and 1606.7 cm-1 come from the C=C stretching vibration of the aromatic ring. Meanwhile, XPS is used to analyze the composition of the material. Fig shows the XPS spectra of Fe_3O_4/PDA vesicle nanospheres. The characteristic peak at 707.5 eV and 720.9 eV belong to the binding energy of Fe 2p3/2 and 2p1/2. There is no satellite peak between the Fe 2p3/2 and 2p1/2 peak, showing the existence of Fe_3O_4.The peak at 399.08 was attributed to the N 1s from the PDA. These results demonstrated that the Fe_3O_4 core has been coated by PDA shell.

S4: discussion about magnetic loss tangent and dielectric loss tangent

For the composites consisting of magnetic core and dielectric shell, the absorption property closely depends on the magnetic loss. Therefore, the magnetic loss tangents ($\tan \delta_{\mu} = \mu''/\mu'$) of the all samples are calculated (Fig S10). The magnetic loss tangent stand for the attenuation capability of electric and magnetic energy. It was found that the all samples exhibit similar increasing tendency in the range of 2-18 GHz, revealing the strong microwave dissipation ability for the composites. Moreover, with the elevated reaction time, the magnetic loss tangents correspondingly improved. The tendencies of $\tan \delta_{\mu}$ values from Fe_3O_4/PDA vesicle series are in accord with the microwave absorption performances. In addition, the dielectric loss tangents (tan $\delta_\varepsilon = \varepsilon''/\varepsilon'$) are calculated, the maximum values of tan δ_μ for the five samples are 0.2682, 0.3625, 0.3819, 0.4170, 0.4418, and the tan δ_ε are 0.5649, 0.6921, 0.5667, 0.5025, 0.5119, respectively. Generally, the excellent microwave absorptions are strongly dependent on the efficient complementarities between the relative permittivity and permeability. The EM impedance matching is more satisfied in the Fe_3O_4/PDA vesicle-5 compared to other samples, the Fe_3O_4/PDA vesicle-5 exhibits ultra-wide bandwidth(11.6 GHz) and strong absorption(-50 dB). The all results match the variation tendency of performance consistently.

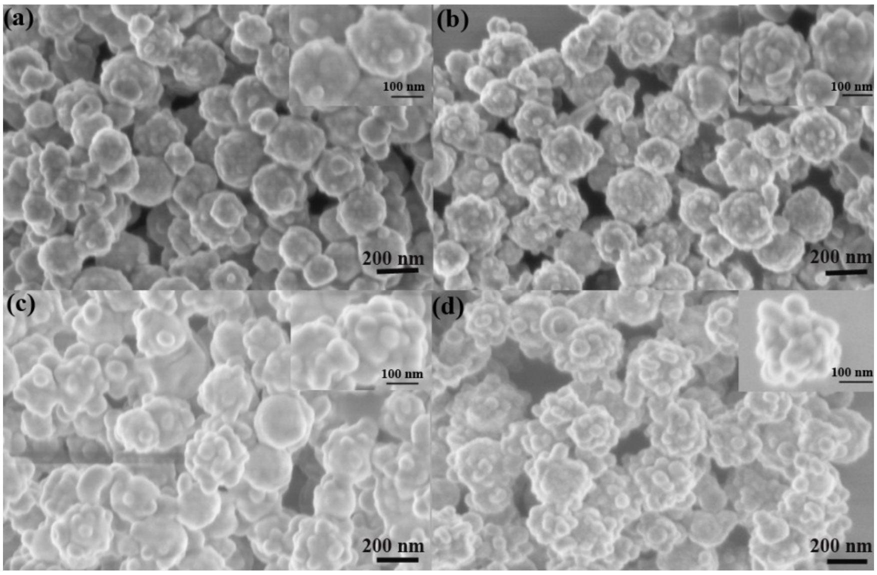

Fig S1. SEM images of Fe_3O_4/PDA vesicle Janus nanospheres at different reaction time. (a) 2h, (b) 3h, (c) 5h, (d) 6h.

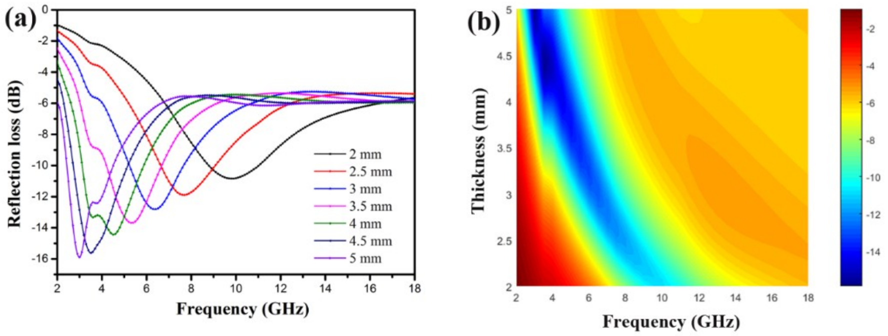

Fig S2. (a) Frequency dependence of microwave RL curves of Fe_3O_4 nanospheres. (b) 3D representation of reflection loss (RL) values of Fe_3O_4 nanospheres.

Sample	Optimal RL (dB)	Frequency range (GHz) (RL < –10dB)	Reference s
Fe_3O_4@SnO_2	-22.6	10.0-12.2	1
Fe_3O_4@TiO_2	-33.4	4.3-12.1	2
Fe_3O_4@C	-20.6	11.8-15.6	3
Fe_3O_4/GCs	-32	5.4-17.0	4
γ-Fe_2O_3@ C@ α-MnO_2	-41.7	7.48-16.66	5
Ni@void@SnO_2	-29.7	8.5-17.6	6
CoNi@SiO_2@TiO_2	-58.2	7.7-13.2	7
Fe_3O_4@CuSilicate	-23.5	3.5-13.9	8
NiO@graphene	-59.6	12.84-16.72	9

Table S1. Microwave absorption performances of some core/shell composites.

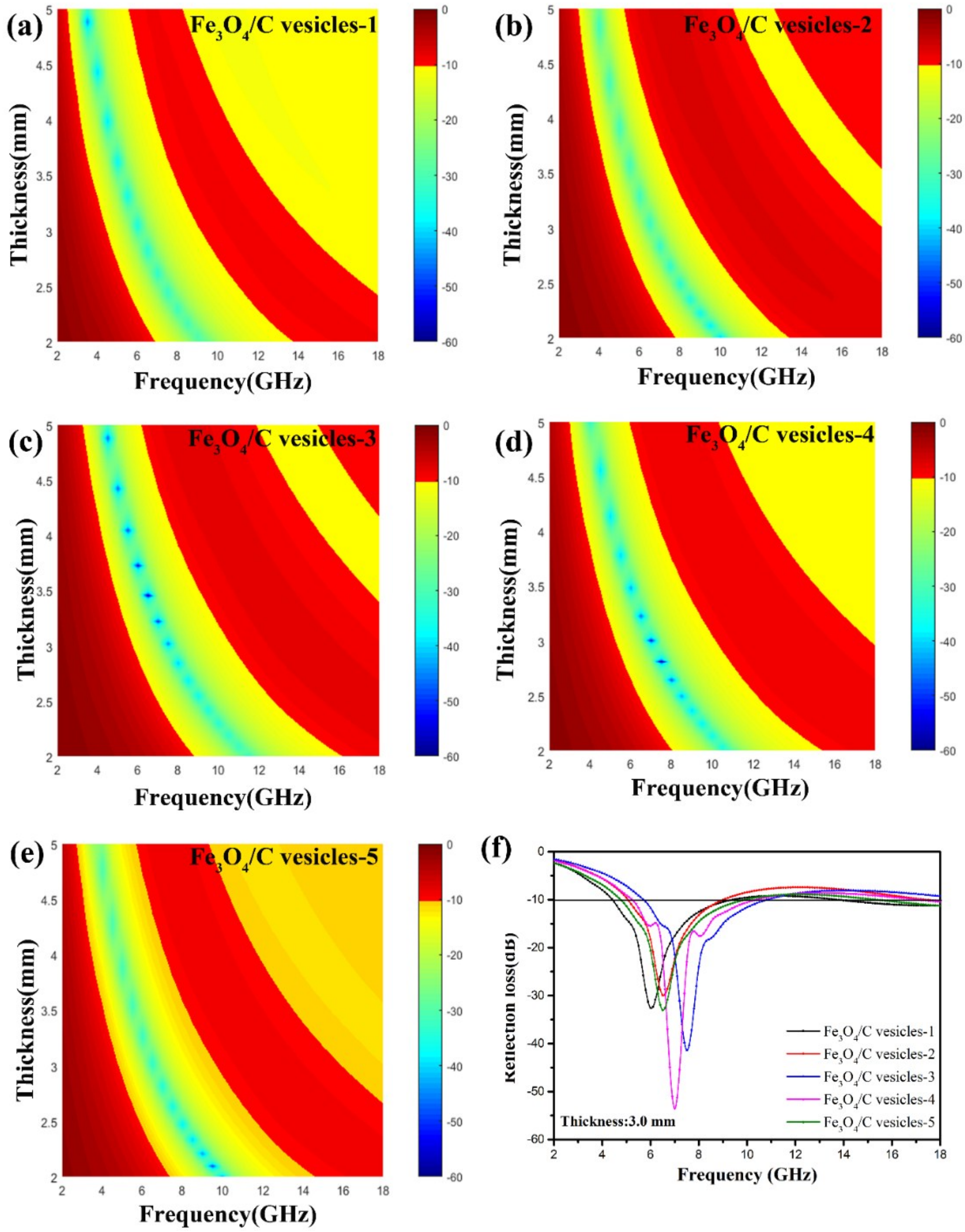

Fig S3. 3D representations of reflection loss (RL) values of a) Fe_3O_4/C vesicles-1, b) Fe_3O_4/C vesicles-2, c) Fe_3O_4/C vesicles-3, d) Fe_3O_4/C vesicles-4, e) Fe_3O_4/C vesicles-5. f) Frequency dependence of microwave RL curves of the Fe_3O_4/C vesicles series at the thickness (3.0 mm)

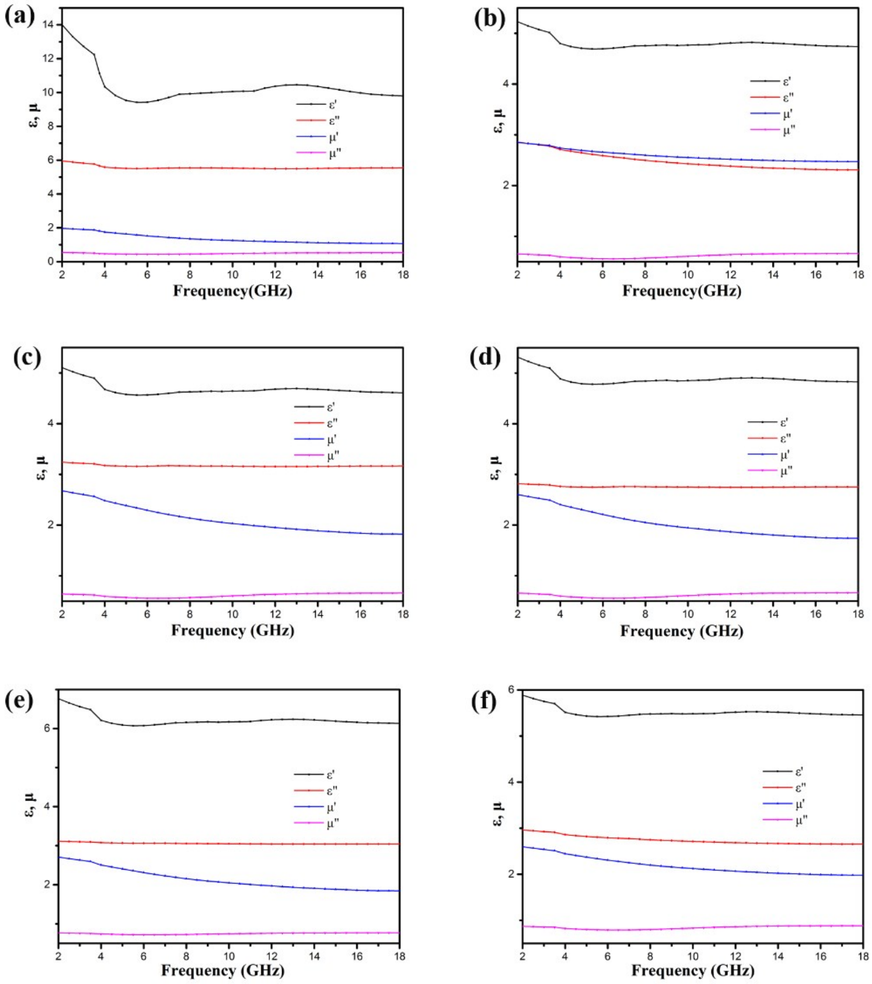

Fig S4. Frequency dependence of the real and imaginary parts of complex permittivity (ε) and permeability (μ) of the (a) Fe_3O_4, (b) Fe_3O_4/PDA vesicles-1, (c) Fe_3O_4/PDA vesicles-2, (d) Fe_3O_4/PDA vesicles-3, (e) Fe_3O_4/PDA vesicles-4, (f) Fe_3O_4/PDA vesicles-5.

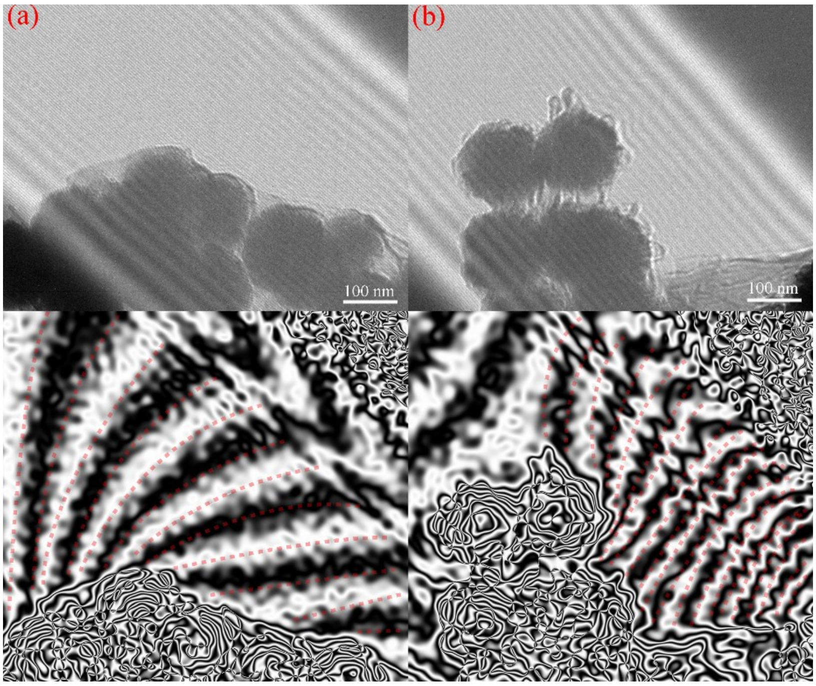

Fig S5. Off-axis electron holograph of Fe_3O_4/PDA vesicle Janus nanospheres.

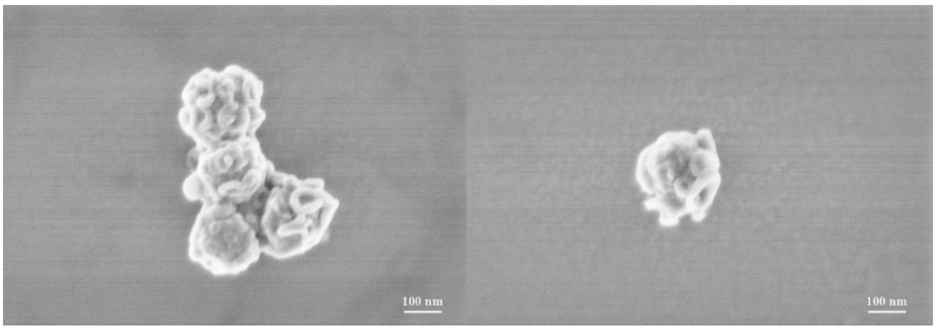

Fig S6. SEM of the Fe_3O_4/PDA vesicle Janus nanosphere.

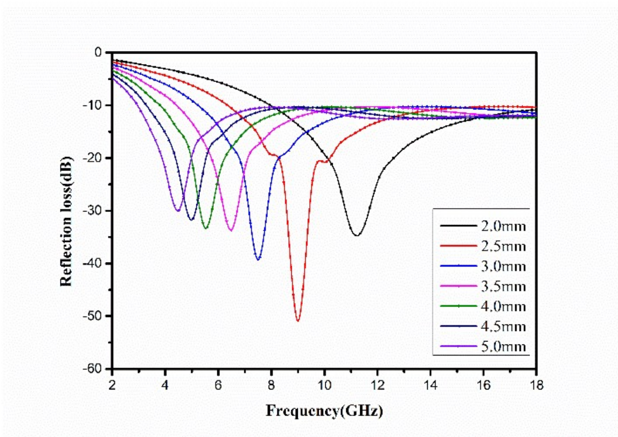

Fig S7. 2D RL images of Fe_3O_4/PDA vesicle-5 with the thicknesses from 2.0 to 5.0 mm

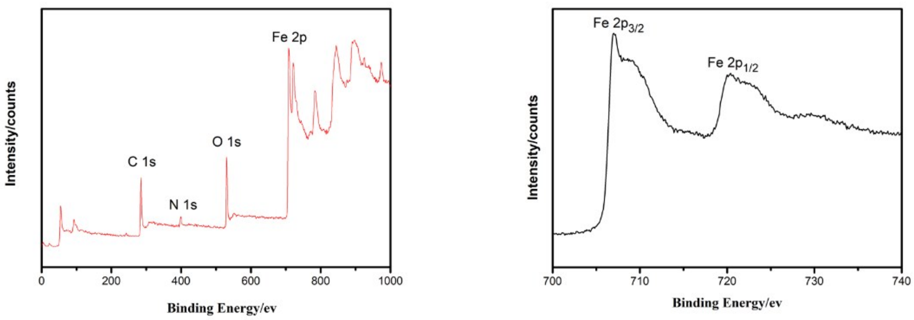

Fig S8. XPS spectrum of the Fe_3O_4/PDA vesicle Janus nanosphere.

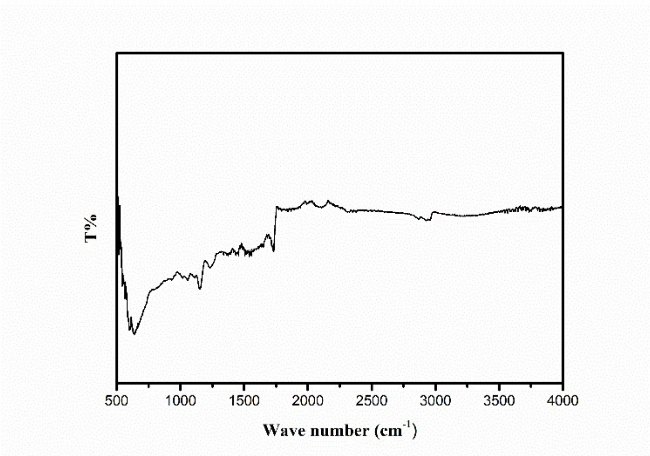

Fig S9. FTIR spectrum of the Fe_3O_4/PDA vesicle Janus nanosphere.

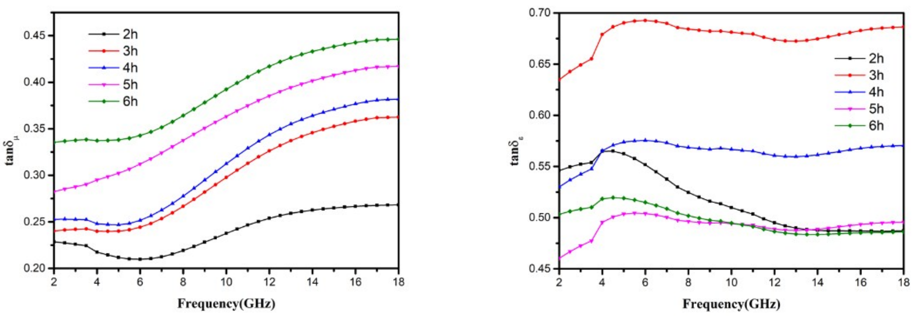

Fig S10. Frequency dependence of magnetic loss tangents and dielectric loss tangents of the Fe_3O_4/PDA vesicle Janus nanosphere.

Supplementary references

1 J. Liu, J. Cheng, R. Che, M. Liu and Z. Liu, Double-shelled yolk–shell microspheres with Fe3O4 cores and SnO2 double shells as high-performance microwave absorbers, J. Phys. Chem. C, 2012, **117**, 489-495.

2 J. Liu, J. Xu, R Che, H. Chen. M. Liu and Z. Liu, Hierarchical Fe3O4@ TiO2 Yolk–Shell Microspheres with Enhanced Microwave-Absorption Properties[J]. Chemistry-A European Journal, 2013, **19**, 6746-6752.

3 Y. Du, W, Liu, R. Qiang, Y. Wang, X. Han, J. Ma and P. Xu, Shell Thickness-Dependent Microwave Absorption of Core–Shell Fe_3O_4@C Composites, ACS Appl. Mater. Interfaces, 2014, **6**, 12997-13006.

4 X. Jian, B. Wu, Y. Wei, S. Dou, X. Wan and W. He, Facile synthesis of Fe3O4/GCs composites and their enhanced microwave absorption properties. ACS Appl. Mater. Interfaces. 2016, **8**, 6101-6109.

5 W. You, H. Bi, W. She, Y. Zhang and R. Che, Dipolar-Distribution Cavity γ-Fe_2O_3@ C@ α-MnO2 Nanospindle with Broadened Microwave Absorption Bandwidth by Chemically Etching, Small, 2017, **13**.

6 B. Zhao, X. Guo, W. Zhao, J. Deng, B. Fan, G. Shao and R. Zhang, Facile synthesis of yolk–shell Ni@ void@ SnO_2 (Ni_3Sn_2) ternary composites via galvanic replacement/Kirkendall effect and their enhanced microwave absorption properties, Nano Res., 2017, **10**, 331-343.

7 Q. Liu, Q. Cao, H. Bi, C. Liang, K. Yuan, W. She, Y. Yang and R. Che, CoNi@ SiO_2@ TiO_2 and CoNi@ Air@ TiO_2 microspheres with strong wideband microwave absorption, *Adv. Mater.*, 2016, **28**, 486-490.

8 J. Liu, J. Xu, Z, Liu. X. Liu and R. Che, Hierarchical magnetic core-shell nanostructures for microwave absorption: synthesis, microstructure and property studies. Science China Chemistry, 2014, **57**, 3-12.

9 L. Wang, H. Xing, S. Gao, X. Ji and Z. Shen. Porous flower-like NiO@ graphene composites with superior microwave absorption properties. J. Mater. Chem. C, 2017, **5**, 2005-2014.